Local charge distortion due to Cr in Ni-based concentrated alloys

Jacob Fischer and Dilpuneet S. Aidhy*

Department of Materials Science and Engineering, Clemson University, Clemson SC 29634

*Corresponding author email: daidhy@clemson.edu

Abstract

Due to the presence of multiple elements consisting of a range of atomic radii, local lattice distortion (LLD) is commonly observed in concentrated (and high entropy) alloys. However, since these elements also have diverse electronegativities, recent works show that atoms can have a range of atomic charges. In this work, using density functional theory (DFT), we investigate electronic charge distribution in face centered cubic (FCC) Ni-based alloys and find significant charge-density distortion in HEAs. Specifically, Cr atoms have large charge density distortion that results in a wide range of bond lengths, atomic charges, and electronic density of states in Cr-containing alloys. The charge distortion impacts the stacking fault energies (SFEs) as a wide range of SFEs are observed in Cr-containing alloys (e.g., NiCr, NiFeCr and NiCoCr), which are otherwise narrow and converged in non-Cr containing alloys such as NiFe, NiCo and NiFeCo. These observations provide insights into the role of local charge distortion towards local lattice distortion in HEAs and illustrate the effect of charge distortion on the mechanical properties of the alloys.

1. Introduction

The co-presence of multiple principal elements in high entropy alloys (HEAs) in equi- or near-equiatomic proportions have opened a vast compositional space for materials design. These alloys have unique properties including cryogenic-temperature ductility [1,2], superior mechanical behavior at elevated temperatures [3], high radiation damage tolerance [4,5], superconductivity [6], and magnetic behaviors [7,8]. The chemical randomness in HEAs, characterized by the random distribution of elements on the crystal lattice, leads to a wide variety of distinct nearest-neighbor (NN) environments. Additionally, the disparity among the atomic radii of the elements leads to the displacement of atoms from their ideal lattice sites creating bond length variations. The NN environment and atomic radii collectively lead to a distorted lattice, termed as local lattice distortion (LLD), that has been observed both experimentally and computationally [9–11]. The interaction of LLD with dislocations is presumed to enhance alloy strength and is considered analogous to solid solution strengthening in conventional alloys [12].

Recent DFT calculations have further revealed that the atomic radius of an element is correlated to its NN environment. Specifically, due to the range of electronegativities of various alloying elements, different atoms of a given element experience different amounts of charge transfer that cause variations in their atomic radii [13]. The DFT calculations also suggest that the atomic displacement is closely linked to the charge transfer. For example, it has been shown that the elements that gain electrons have smaller atomic displacements and vice versa [14]. Thus, there is an emerging understanding that the atomic radius and charge transfer collectively lead to LLD.

Although charge transfer is normally quantified as a scalar value (e.g., via Bader segmentation in DFT), the spatial distribution of the electronic charge, especially its asymmetric distribution, emerges as an important parameter in the chemically random environments. This asymmetric distribution leads to localized distortions in the charge density, a phenomenon we refer to as local charge distortion (LCD). The charge distortion has been used to explain many properties including stacking fault energies (SFEs) in alloys. It has been postulated that large variations in SFEs can be attributed to the asymmetric charge distribution that could impose resistance to planar shearing in specific crystallographic directions [15–19]. Charge distortion has also been used to explain unintuitive vacancy diffusion in metals [20] where, unintuitively, larger atoms have lower migration barriers due to easier charge reorientation at the saddle point. In addition, charge distribution is often used as a descriptor to probe surface/catalytic properties [21–23].

Recent DFT calculations by Oh et al. [14] analyzed charge transfer among the five elements in a face-centered cubic (FCC) Cantor alloy. It is found that the charge transfer follows the electronegativity trend, i.e., lower electronegative elements lose charge. For example, all Cr atoms lose charge due to their lowest electronegativity among all of the alloying elements. However, it was also found that the Cr atoms show the largest variation of valence charges (in terms of Bader charge) among its atoms compared to the other four elements. In addition, a significantly larger LLD around Cr, measured in terms of bond length, was previously observed by Okamoto et al. [24]. Recent work from our group also indicated an enhanced asymmetric charge distribution around Cr atoms in binary and

ternary Ni-based model alloys compared to other elements [25,26]. The underlying reason is likely the partially filled *d*-shell electron of Cr granting greater electronic deformation flexibility [27]. Previous DFT calculations show that this enhanced flexibility induces larger variations of Cr point-defect energies compared to Ni and Co.

Motivated by these observations, in this work, we examine LCD in Ni-based binary and ternary alloys in Ni-Fe-Co-Cr compositional space using DFT calculations. We relate the electronic distortion to SFE variations in various dilute and concentrated alloys. Specifically, we show that (1) LLD and charge distortion are correlated, (2) there is much higher LCD around Cr atoms compared to other elements, (3) the presence of Cr causes much larger LLD, and (4) the larger LCD and LLD result in larger variations of SFEs. Based on these results, we propose that the amount of charge distortion is an important factor that affects the LLD and hence SFE. The alloys with symmetric charge distribution exhibit a narrow range of SFE in contrast to a larger variation in Cr-containing alloys.

2. Methodology

2.1 DFT calculations

The DFT calculations are performed using Vienna ab initio simulation package (VASP) code [28–30]. The full potential frozen-core project-augmented wave (PAW) is used to describe the electron-ion interactions along with the generalized gradient approximation (GGA) with Perdew-Burke-Ernzerhof (PBE) exchange correlation functional [31]. Figure 1a-c displays the FCC supercells with a total of 108 atoms distributed on nine atomic layers. Figure 1a shows the 'dilute' structure containing only six alloying elements added only on the 5th layer. Figure 1b shows another dilute structure containing two different alloying elements, three atoms of each element in the 5th layer. Finally, Figure 1c is a concentrated special quasirandom structure (SQS) containing equiatomic ternary composition with alloying elements in all nine layers. The nine layers are parallel to the (111) plane and a 6 Å vacuum is applied to prevent the interaction between the top and bottom layers. The SQS structures are generated using the Alloy Theoretic Automated Toolkit (ATAT) software [32]. The Brillouin zone sampling is employed by the Monkhorst-Pack method with a $6 \times 6 \times 1$ k-point mesh. A plane wave energy cutoff of 350 eV is set, with total energy convergence within 1×10^{-4} eV and internal atomic position forces relaxed to less than 1×10^{-2} eV. The Methfessel-Paxton method is implemented using a smearing width of 0.1 eV. Collinear spin-polarized calculations are performed with a ferromagnetic (FM) configuration. All atoms are initialized with a magnetic moment of 3 μ_B. Both the dilute and SQS structures share this initial setup, but the magnetic moment of Cr exhibits a contrasting behavior once the final magnetic order has been determined. Upon relaxation, in dilute alloys, Cr adopts a FM alignment, deviating from its characteristic antiferromagnetic (AFM) behavior observed in the SQS structures. This shift in magnetic order is likely driven by the strong influence of the surrounding FM Ni atoms, which have high concentration compared to the Cr atoms that are sparsely distributed on the 5th layer of the dilute structure. Our findings agree with the observations of Niu et al. [33], who noted a strong influence of neighboring elements on Cr magnetic moments within NiCoCr and NiCoFeMnCr structures. Additionally, the final magnetic moment distributions for the SQS structures are also in good agreement with those obtained using established DFT methods [33–37]. This agreement includes

the expected positive moments for Ni, Co, and Fe, while Cr exhibits a distribution of both positive and negative moments. To further explore the electronic charge distribution for each alloy, we apply the Bader Charge Analysis method, which leverages the Quantum Theory of Atoms in Molecules (QTAIM) theory [38]. This technique, developed by Henkelman et al. [39], provides an approximation of the total electronic charge on each atom. The variation in Bader charges serves as a metric to assess charge asymmetry. Charge loss reduces the atomic radius, while charge gain enlarges it, leading to LLD. A wide range of Bader charges for a given element results in significant charge density distortion.

2.2 Stacking fault energy

A slab deformation approach is used to generate an intrinsic stacking fault (ISF) along $\{111\}[11\bar{2}]$ for each supercell. The first four layers (from bottom to top) are fixed in their original position while the remaining layers are displaced in the $[11\bar{2}]$ direction creating an ISF along the 5th layer. Additionally, this leads to a change in the stacking sequence from *ABCABCABC* to *ABCACABCA*.

The initial bulk structure is first relaxed to fully optimize the atomic positions, cell shape, and cell volume of the supercell. Then, a vacuum is applied to both the perfect (non-sheared) and sheared structures for further relaxation, while constraining the cell shape volume. The SFE is then calculated using Eq. (1),

$$E_{SFE} = \frac{E_{sheared} - E_{perfect}}{A_{SF}} \tag{1}$$

where $E_{sheared}$ and $E_{perfect}$ are the energies for the perfect and sheared supercells, and A_{SF} is the cross-sectional area of the ISF. For the dilute structures, the host atoms on the 5th layer are substituted with various alloying atoms to calculate SFE using a standard method in literature [15,40–42]. In concentrated SQS structures, the SFE is calculated individually for each of the nine layers. Preliminary testing in pure Ni resulted in a calculated intrinsic SFE of 136.94 mJ/m^2, which is in good agreement with previous DFT results [15,43]. The calculated SFEs for concentrated ternary alloys in this study also fall within the range of values reported in prior literature [44,45].

The lengths of the lattice vectors **a**, **b**, and **c** of the orthorhombic cell are $a_0\sqrt{3/2}$, $a_0/\sqrt{2}$, and $a_0\sqrt{3}$ where a_0 is the lattice parameter of the FCC structure. The supercell is constructed with an initial lattice parameter of 3.52 Å, consistent with prior research [46,47]. Relaxation of the FCC unit cell converged to an average lattice constant of 3.514 Å, which falls within the range reported in previous studies [44,46–49]. Additionally, the converged average lattice constants for the NiFeCo, NiCoCr and NiFeCr concentrated alloys were found to be 3.547, 3.520, and 3.549 Å which are consistent with existing literature [44,50]. Multiple atomic configurations of both dilute structures (Figures 1a and 1b) are modeled to capture statistical variations. We recognize that the limited configurations do not encompass all possible configurations. However, they enable us to study the qualitative effect of Cr, which is the main goal of this work. We also acknowledge that magnetic fluctuations could possibly impact the observed SFE ranges, and our

configurations may not capture a complete range of SFEs as this range can be very wide, observed in previous works [44,45,51].

2.3 Image processing of charge distortion

In this paper, LCD is interpreted through various methods, including visual mapping of the charge distortion from charge density images, Bader charges, and bond lengths. However, it is explicitly calculated using ImageJ analysis, where the atomic areas of each element are measured. Significant variation in these areas, due to different amounts of charge transfer from various nearest neighbor environments, leads to larger LCD. The analysis of the charge distribution is performed by collecting charge density data from the CHGCAR file after full relaxation of the supercell. The data encompasses all layers normal to the $\langle 111 \rangle$ direction. For the dilute structures, we focus on the data from the 5^{th} layer to examine the charge distribution variations around the embedded alloying elements. In concentrated structures, all nine layers are analyzed. After data collection, contour plots are generated to visualize the charge density distribution within a chosen layer. Previous work in our group has used this technique to predict SFE using a convolutional neural network (CNN) model with charge density as a main descriptor [25,26]. In this work, we quantify the charge distortion via image processing.

The charge density images are prepared using a code from the sisl Python module [52]. The 800 x 500 pixel images display the distribution of charge at the center and surrounding an atom, as shown in Figures 2a and 2b. These images are processed using the open-source platform ImageJ/Fiji [53]. The software has been used to obtain quantitative data from images in other fields such as biology and medicine. For example, leveraging the functionality of ImageJ/Fiji, Pijuan et al. [54] assessed cell migration behavior to facilitate physiological and cellular characterization. It has also been utilized in materials science applications to analyze particles of varying sizes. For example, Boley et al. [55] use ImageJ to characterize the particle sizes of mechanically sintered Ga-In nanoparticles. In this study, we employ ImageJ/Fiji to quantify the charge distribution of the atoms to capture geometric changes that occur due to variations in LCD. The preprocessed images shown in Figure 2a and 2b offer a visual representation of the charge distribution of one individual atom. The black and white regions highlight the charge density maxima and minima, respectively. Red-yellow gradients signify the charge transfer between atoms.

The images are first converted to an 8-bit grayscale with 256 levels of intensity. A threshold range is then set to separate the background area from the particle region. To capture the edges of the black region in Figure 2, a manual thresholding process was implemented. Optimal segmentation was achieved for each image set by iteratively adjusting the threshold based on visual comparisons with the original image. This process considered factors such as particle size, shape and the overall image contrast to exclude the red-yellow halo surrounding the central atom. While this approach provided satisfactory results, automated thresholding techniques could be explored in future studies to enhance reproducibility and efficiency. The next step involved using ImageJ/Fiji's particle analysis package to compute the area of the concentrated charge, accurately capturing the geometric variation for each atom. The comparison of Figures 2a and 2b depicts the contrasting geometries that can occur in these alloys and highlights

the extent of LCD. Figures 2c and 2d show an example of the processed image that is used to capture the area of the atoms. As shown later, a significant difference in the atomic area is observed for different elements, that is correlated to LLD.

3. Results

3.1 Charge density distortion in dilute binary alloys

The charge density distributions of the 5th layer corresponding to Figure 1a in ten different supercells are shown in Figure 3. The corresponding SFEs calculated at the 5th layer in all supercells are shown in Table 1. Note that each supercell consists of six atoms of an alloying element (i.e., either Co, Fe, or Cr) in the 5th layer while the remaining atoms are all Ni. The only difference among the supercells is the arrangement of the alloying atoms during the initial setup to the DFT calculation. It is observed that all ten configurations in both NiCo and NiFe alloys display symmetrical charge distributions suggesting minimal LCD as shown in Figures 3a and 3b, respectively. In addition, there is an almost negligible difference in the charge distribution between Ni and Co atoms, and there is subtle difference between Ni and Fe atoms. This uniform distribution sharply contrasts with NiCr alloys in Figure 3c, which display significant variations in charge density at three different levels: across ten configurations, between Ni and Cr atoms of a given configuration, and among Cr atoms of the same configuration. For example, the charge densities of configurations C2, C4, C6, C7, C8, C9 and C10 have larger variations whereas that in configurations C1, C3 and C5 show little to no variation. The configurations with high variation exhibit pronounced distortion around Cr atoms, indicative of larger LCD. In contrast, Ni atoms experience minimal distortion. While some Cr atoms appear circular (such as in C1 and C3), others exhibit an elliptical or even a quadrilateral geometry (such as in C6 and C9). Such wide variations and differences among the alloying elements are not observed in NiCo and NiFe. These results indicate that there is significant LCD around Cr atoms.

Interestingly, it is noted that there is a correlation between the LCD and SFE variation. While the SFE variation in NiCo and NiFe is small, i.e., with a standard deviation (σ) of ±1.1 mJ/m^2, NiCr exhibits a significantly larger spread with a σ of ±24 mJ/m^2 as shown in Table 1. The effect of LCD is further observed in the DOS of the alloying elements in each supercell, as shown in Figure 4. In NiCo, among all ten configurations, there is very little variation of the Co DOS at the Fermi level, as shown in Figure 4a, and there is minor variation among the Fe atoms, as shown in Figure 4b. Figure 4c, however, illustrates the diverse profiles of the Cr DOS in NiCr, reaffirming the larger charge density distortion. These results indicate that the configurational placement of alloying element is not the main cause of variations in the SFEs. Instead, the observed variations are attributed to the differences in charge density distribution.

The LCD around Cr is also evidenced in the valence charge of the atoms quantified by Bader charge. Figure 5 shows the Bader charge distribution of all Co, Fe and Cr atoms among all ten configurations plotted against their respective SFEs. Vertical and horizontal error bars for each alloy dataset represent the standard deviation of SFE and Bader charge, respectively. The midpoint indicates the value for the average SFE and Bader charge. Due to the lowest electronegativity of Cr, it loses the largest amount of charge.

The charge lost by Co and Fe atoms is relatively smaller, and because Co has higher electronegativity than Fe, they lose smaller charge than Fe atoms. In all alloys, the Ni atoms gain charge due to their highest electronegativity, as shown in Figure 5. The distribution of the Bader charges of the alloying elements illustrates charge distortion; while the Bader charges of Co and Fe atoms are similar and clustered, that of the Cr atoms is scattered, illustrating the variability of charge distribution around Cr atoms. The wider distribution of Ni Bader charges is only in NiCr structure and is due to the Bader charge distribution of the Cr atoms.

It is further observed that there is a correlation between LCD and LLD. Figure 6 shows the bond length distribution of all possible bonds in the three alloys. The probability density is estimated using kernel density estimation (KDE) with Gaussian kernels. Figures 6a, 6b and 6c show Ni-Ni, Ni-X and X-X bond lengths in the three alloys, respectively, where X denotes Co, Fe or Cr. In NiCo and NiFe, a smaller variation among Ni-Ni bond lengths is observed; the σ of the variation is less than 0.007 Å, in Figure 6a. The σ is relatively higher in NiCr, i.e., 0.015 Å. In Figure 6b, the Ni-X bond length variation increases consistently in all three alloys compared to the corresponding Ni-Ni bonds. The variation is highest in Ni-Cr followed by Ni-Co and Ni-Fe. However, the X-X variation shows the most dramatic difference, as shown in Figure 6c. The Cr-Cr bonds have a very large variation (σ = 0.079 Å) compared to Co-Co and Fe-Fe bond lengths (σ = 0.014 Å and σ = 0.027 Å, respectively). These results reinforce the observation that Cr has much larger distortion in its NN environment compared to Co and Fe. In addition, collectively, Figures 4 and 5 indicate that LCD and LLD are likely corelated.

Even in very dilute structures, Cr has a profound effect on the charge-density distribution and SFEs. DFT calculations are performed in supercells containing only two alloying elements in the 5th layer. Two calculations for each alloying element are performed, distinguished by the placement of the atoms as the first nearest-neighbors (1NN) and third nearest-neighbors (3NN). The 3NN configuration is presumed to nullify (or reduce) the Cr-Cr interaction, within the constraints of the DFT supercell size. Among all three structures, the 3NN configuration has a lower total energy than 1NN which indicates that it is the preferred configuration. Minimal variation in both charge density and SFE is observed in Co and Fe structures in both 1NN or 3NN configurations as shown in Figures 7a and 7b, respectively. However, the structures containing Cr show a significant difference in both local charge density and SFE. A higher charge density is observed between the two Cr atoms in the 1NN configuration as shown in Figure 7c. The DOS also reflects the trend observed for the atomic arrangements. Minimal variation is exhibited in the Co and Fe structures, while the Cr structures display larger difference. These results demonstrate that, even in the most dilute structures, the placement of Cr atoms can have a significant effect on its surrounding charge-density landscape.

3.2 Charge density distortion in dilute ternary alloys

To understand the effect of Cr in the presence of other alloying elements, three ternary alloys i.e., NiFeCo, NiCoCr, and NiFeCr are investigated. The supercells resemble binary structures, with alloying elements solely in the 5th layer. Three atoms of each alloying element are added, leading to a total of six alloying atoms. The charge density distributions of NiFeCo, NiCoCr, and NiFeCr are shown in Figures 8a, 8b and 8c,

respectively. Consistent with previously discussed results, minor charge distortion is observed in NiFeCo in Figure 8a. Figure 8b shows larger variations in the charge density distributions in NiCoCr with severe distortion around Cr-Cr bonds such as in configurations C1, C3 and C5. This charge distortion and Cr correlation becomes evident during comparison between NiFeCo and NiFeCr, as shown in Figures 8a and 8c, respectively. Although the Ni and Fe atoms have the same atomic placements in both structures, the charge density distributions are dissimilar. In NiFeCo, all eight configurations exhibit similar charge density distributions regardless of the arrangement of Fe and Co atoms. In contrast, the presence of Cr atoms in NiFeCr leads to larger LCD compared to NiFeCo. The configurations with more Cr-Cr bonds seem to coincide with larger LCD. This warrants further investigation pertaining to the influence of Cr-Cr bond interaction. Interestingly, the LCD is not confined to the immediate vicinity of Cr atoms indicating a more extensive spatial influence. The presence of Cr atoms disrupts the symmetrical charge density distribution, leading to more asymmetry around Ni and Fe atoms as well. The configurations C1, C3 and C5 display a particularly pronounced distortion. This increased distortion leads to a notable increase in LCD in Ni and other alloying elements, which becomes more evident in concentrated alloys presented later. Compared to non-Cr counterparts like NiFeCo, alloys containing Cr exhibit larger variations in SFE, as shown in Table 2.

The DOS plots also show larger variation in Cr alloys, as shown in Figure 9. While little to moderate DOS variation occurs for Co and Fe atoms as observed in Figures 9a, 9b, 9c and 9e, a much larger variation is observed for Cr atoms, as shown in Figures 9d and 9f. This substantial DOS difference of Cr atoms indicates the presence of charge density distortion due to Cr even in multi-elemental alloys.

Figure 10 illustrates the Bader charge and SFE in the three structures. As demonstrated in binary compositions, the ternary compositions show larger Bader charge variation in Cr containing compositions NiFeCr and NiCoCr, whereas little variations are observed in NiFeCo. Similarly, there is greater SFE variation in the Cr-containing structures. The bond length variations, as illustrated in Figure 11, are likely a consequence of the observed charge distortions. For example, the Ni-Ni bonds in NiFeCo have a relatively narrower distribution (and higher peak) compared to the two Cr-containing compositions displayed in Figure 11a. Similarly, the Ni-Fe bonds have wider variation in NiFeCr compared to NiFeCo, as shown in Figure 11b. Figure 11c shows that Ni-Cr bonds have larger distortion both in NiFeCr and NiCoCr compared to Ni-Co bonds in NiFeCo. The distribution of Co-Co and Fe-Fe bond lengths, shown in Figures 11d and 11e, exhibit smaller variation compared to Cr-Cr bonds. The Co-Cr and Fe-Cr bonds in Figure 11f demonstrate a larger distortion than Fe-Co bonds. These results are an initial indication that in multi-elemental alloys, Cr could demonstrate wider ranges across all bond types. We conclude that while the non-Cr compositions display moderate fluctuations due to LLD caused by atomic radii differences, the larger distortions observed in Cr-containing alloys are likely caused by the combined effect of LLD and LCD, and the latter has a significant contribution to the overall distortion.

3.3 Charge density distortion in concentrated ternary alloys

Finally, the charge density distortion is analyzed in concentrated equiatomic ternary alloys. The supercells consist of equal concentration of three elements in all nine layers constructed in SQS. The trends of lattice and charge distortions not only translate into SQS structures, i.e., the Cr containing alloys have larger bond length, Bader charge and SFE variations, but the variations are also more pronounced. The charge density distributions of all nine layers of each SQS structure of NiFeCo, NiCoCr, and NiFeCr are shown in Figures 12-14, and the corresponding SFEs are shown in Table 3. Smaller LCD is observed in Co and Fe atoms, as shown in Figure 12. In contrast, the NiCoCr and NiFeCr structures demonstrate diverse charge distributions in each atomic layer and exhibit a wide range of SFEs that lie in both positive and negative range of values. Such variations in NiCoCr have been widely observed in previous DFT studies [44,45]. The LCD is more prevalent around Cr atoms and irregular shapes of Cr atoms are observed in Figures 13 and 14. Due to higher concentration of the alloying elements, there is a wider distribution of SFEs and Bader charges as demonstrated by Figure 15. Figure 16 shows a significant increase in bond-length variations compared to dilute ternaries in Figure 11, especially in Cr-containing compositions. The effect of Cr on bond length variation is evident in all bond lengths, especially in Cr-Cr bonds as shown in Figure 16.

Due to higher concentration of the alloying elements, there is larger charge distortion evident in the shape of the atoms. The irregular shapes of the atoms are quantified by image analysis using ImageJ/Fiji software [53]. Specifically, the area occupied by the charge density of an atom, obtained from the pixel occupancy, is calculated. Figure 17 shows the data for all alloys in dilute-binary, dilute-ternary and concentrated-SQS structures. Due to higher symmetry (and little distortion), Figure 17a shows a narrow distribution of atomic areas of Ni and Co atoms. It is also observed that Co atoms are larger than Ni atoms, which is consistent with their metallic radii. Similar narrower distribution is observed in Ni and Fe atoms in Figure 17b. In contrast, a much wider distribution is observed in Cr atoms in Ni-Cr alloy shown in Figure 17c, as expected based on the above results.

The distribution widens in dilute ternaries in Cr-containing alloys as shown in Figures 17e and 17f, compared to narrow distribution in NiFeCo as shown in Figure 17d. Interestingly, there is almost no difference between the distributions of binary and dilute ternary compositions as shown in Figures 17a, 17b and 17d. This indicates that the substitution of Co and Fe atoms does not have a significant effect on LCD. In contrast, a significant difference is observed between Cr-containing alloys; the area distribution increases not only for Cr atoms, but also for Ni, Co and Fe, as shown in Figures 17e and 17f compared to binary alloys. Finally, in the concentrated SQS structures, the variations further increase in Cr-containing alloys, as shown in Figures 17h and 17i, in agreement with the above results. In NiFeCo, the variations widen compared to binary counterparts as shown in Figure 17g, but the widening is not as large as in NiFeCr. The LLD and LCD effects are observed in the SFE values in Table 3; although, due to higher concentration of alloying elements, the SFE variations are larger in all three alloys, but they are significantly larger in Cr-containing NiCoCr and NiFeCr alloys illustrating the additional contribution of LCD.

4. Discussion

In this work, the effects of LCD in Ni-based alloys have been studied with particular emphasis on its correlation to SFE variation using DFT calculations. In previous studies, wide ranges of SFEs have been observed in HEAs using DFT methods [45,56–58]. It has been established that this observation is due to the extensive chemical disorder and unique nearest-neighbor environments often found in these alloys. The new results in this work illustrate that the charge density distortion can also have a significant impact on SFE. In NiCo, NiFe, and NiFeCo structures, there are no notable differences in the LCD or SFE despite diverse atomic configurations. Conversely, Cr-containing compositions have wider SFE variations because they exhibit greater charge distortion. As postulated by Zhao et al. [27], Cr has partially filled *d*-orbitals which allows the flexibility to transition from t_{2g} to e_g electronic states that enable easier charge re-distribution. Such redistribution is subdued in other elements. Larger variation of bond lengths and Bader charges due to Cr compared to other elements have been observed that support the findings in this work. Our results demonstrate that the SFE variations that have been observed in previous works can be partly attributed to LCD, rather than solely based on the nearest neighbor environment and LLD. Previously, Zhao et al. [59] reported a significant variation in SFE tied to the charge density distribution in NiCoCr, compared to the minor SFE variations in NiCo. Our findings indicate that the charge distortion around Cr is the underlying cause for the pronounced SFE differences. In one of our recent works, charge density distribution was used as a descriptor for a convolutional neural network (CNN) model to predict SFE in alloys [25,26]. The integration of ImageJ/Fiji processing tools provides detailed insights to the understanding of the mechanisms governing charge and lattice distortion in alloys.

Short-range order (SRO) has been under intense scrutiny in HEA research. Ding et al. [45] had revealed that the SFE has a strong correlation with local ordering. They showed that as the degree of SRO increases, the SFE is more likely to converge to positive values in NiCoCr. Similar results are found experimentally in NiCoCr by Zhang et al. [60] where higher SFE is observed in SRO structures. In view of the results in this work, the charge density distortion in SRO vs non-SRO structures and their effects on SFEs need to be probed, which will constitute our future work. It is possible that a random distribution of Cr could lead to a more pronounced asymmetrical charge distribution, potentially causing these SFE fluctuations in non-SRO structures.

5. Conclusion

In conclusion, the DFT calculations show that there could be significant charge density distortion around Cr atoms in Ni-based HEAs, compared to relatively little distortion around other elements including Ni, Fe and Co. Consequently, larger lattice distortion is observed in Cr-containing alloys, which results in larger variations in SFEs. These results indicate that local charge distortion may have a significant contribution to local lattice distortion in HEAs.

Acknowledgement

The work is supported by the National Science Foundation project # 2302763 titled CDSE: Charge-density based ML framework for efficient exploration and property predictions in the large phase space of concentrated materials. The computational resources are provided by Clemson University's Palmetto cluster.

Conflict of intertest

There is no conflict of interest.

Data availability

The data is available upon request.

References

[1] C. Zhang, Q. Yu, Y.T. Tang, M. Xu, H. Wang, C. Zhu, J. Ell, S. Zhao, B.E. MacDonald, P. Cao, J.M. Schoenung, K.S. Vecchio, R.C. Reed, R.O. Ritchie, E.J. Lavernia, Strong and ductile FeNiCoAl-based high-entropy alloys for cryogenic to elevated temperature multifunctional applications, Acta Mater 242 (2023). https://doi.org/10.1016/j.actamat.2022.118449.

[2] B. Gludovatz, A. Hohenwarter, D. Catoor, E.H. Chang, E.P. George, R.O. Ritchie, A fracture-resistant high-entropy alloy for cryogenic applications, Science (1979) 345 (2014) 1153–1158. https://doi.org/10.1126/science.1254581.

[3] Y.L. Zhao, T. Yang, Y.R. Li, L. Fan, B. Han, Z.B. Jiao, D. Chen, C.T. Liu, J.J. Kai, Superior high-temperature properties and deformation-induced planar faults in a novel L12-strengthened high-entropy alloy, Acta Mater 188 (2020) 517–527. https://doi.org/10.1016/j.actamat.2020.02.028.

[4] M.A. Cusentino, M.A. Wood, R. Dingreville, Compositional and structural origins of radiation damage mitigation in high-entropy alloys, J Appl Phys 128 (2020). https://doi.org/10.1063/5.0024014.

[5] Y. Lin, T. Yang, L. Lang, C. Shan, H. Deng, W. Hu, F. Gao, Enhanced radiation tolerance of the Ni-Co-Cr-Fe high-entropy alloy as revealed from primary damage, Acta Mater 196 (2020) 133–143. https://doi.org/10.1016/j.actamat.2020.06.027.

[6] S.G. Jung, Y. Han, J.H. Kim, R. Hidayati, J.S. Rhyee, J.M. Lee, W.N. Kang, W.S. Choi, H.R. Jeon, J. Suk, T. Park, High critical current density and high-tolerance superconductivity in high-entropy alloy thin films, Nat Commun 13 (2022). https://doi.org/10.1038/s41467-022-30912-5.

[7] T. Zuo, M. Zhang, P.K. Liaw, Y. Zhang, Novel high entropy alloys of FexCo1-xNiMnGa with excellent soft magnetic properties, Intermetallics (Barking) 100 (2018) 1–8. https://doi.org/10.1016/j.intermet.2018.05.014.

[8] T. Zuo, M.C. Gao, L. Ouyang, X. Yang, Y. Cheng, R. Feng, S. Chen, P.K. Liaw, J.A. Hawk, Y. Zhang, Tailoring magnetic behavior of CoFeMnNiX (X = Al, Cr, Ga, and Sn) high entropy alloys by metal doping, Acta Mater 130 (2017) 10–18. https://doi.org/10.1016/j.actamat.2017.03.013.

[9] C. Lee, G. Song, M.C. Gao, R. Feng, P. Chen, J. Brechtl, Y. Chen, K. An, W. Guo, J.D. Poplawsky, S. Li, A.T. Samaei, W. Chen, A. Hu, H. Choo, P.K. Liaw, Lattice distortion in a strong and ductile refractory high-entropy alloy, Acta Mater 160 (2018) 158–172. https://doi.org/10.1016/j.actamat.2018.08.053.

[10] Y.Y. Tan, M.Y. Su, Z.C. Xie, Z.J. Chen, Y. Gong, L.R. Zheng, Z. Shi, G. Mo, Y. Li, L.W. Li, H.Y. Wang, L.H. Dai, Chemical composition dependent local lattice distortions and magnetism in high entropy alloys, Intermetallics (Barking) 129 (2021). https://doi.org/10.1016/j.intermet.2020.107050.

[11] H.S. Oh, D. Ma, G.P. Leyson, B. Grabowski, E.S. Park, F. Kormann, D. Raabe, Lattice distortions in the FeCoNiCrMn high entropy alloy studied by theory and experiment, Entropy 18 (2016). https://doi.org/10.3390/e18090321.

[12] P. Wang, Y. Wu, J. Liu, H. Wang, Impacts of atomic scale lattice distortion on dislocation activity in high-entropy alloys, Extreme Mech Lett 17 (2017) 38–42. https://doi.org/10.1016/j.eml.2017.09.015.

[13] H.S. Oh, S.J. Kim, K. Odbadrakh, W.H. Ryu, K.N. Yoon, S. Mu, F. Körmann, Y. Ikeda, C.C. Tasan, D. Raabe, T. Egami, E.S. Park, Engineering atomic-level complexity in high-entropy and complex concentrated alloys, Nat Commun 10 (2019). https://doi.org/10.1038/s41467-019-10012-7.

[14] H.S. Oh, K. Odbadrakh, Y. Ikeda, S. Mu, F. Körmann, C.J. Sun, H.S. Ahn, K.N. Yoon, D. Ma, C.C. Tasan, T. Egami, E.S. Park, Element-resolved local lattice distortion in complex concentrated alloys: An observable signature of electronic effects, Acta Mater 216 (2021). https://doi.org/10.1016/j.actamat.2021.117135.

[15] S.L. Shang, C.L. Zacherl, H.Z. Fang, Y. Wang, Y. Du, Z.K. Liu, Effects of alloying element and temperature on the stacking fault energies of dilute Ni-base superalloys, Journal of Physics Condensed Matter 24 (2012). https://doi.org/10.1088/0953-8984/24/50/505403.

[16] S.H. Zhang, I.J. Beyerlein, D. Legut, Z.H. Fu, Z. Zhang, S.L. Shang, Z.K. Liu, T.C. Germann, R.F. Zhang, First-principles investigation of strain effects on the stacking fault energies, dislocation core structure, and Peierls stress of magnesium and its alloys, Phys Rev B 95 (2017). https://doi.org/10.1103/PhysRevB.95.224106.

[17] S. Ogata, J. Li, S. Yip, Ideal Pure Shear Strength of Aluminum and Copper, Science (1979) 298 (2002) 807–811. https://doi.org/10.1126/science.1076652.

[18] Y.F. Wu, S. Li, Z.G. Ding, W. Liu, Y.H. Zhao, Y.T. Zhu, Effect of charge redistribution factor on stacking-fault energies of Mg-based binary alloys, Scr Mater 112 (2016) 101–105. https://doi.org/10.1016/j.scriptamat.2015.09.023.

[19] T.L. Achmad, W. Fu, H. Chen, C. Zhang, Z.G. Yang, Computational thermodynamic and first-principles calculation of stacking fault energy on ternary Co-based alloys, Comput Mater Sci 143 (2018) 112–117. https://doi.org/10.1016/j.commatsci.2017.11.004.

[20] M. Krčmar, C.L. Fu, A. Janotti, R.C. Reed, Diffusion rates of 3d transition metal solutes in nickel by first-principles calculations, Acta Mater 53 (2005) 2369–2376. https://doi.org/10.1016/j.actamat.2005.01.044.

[21] R.B. Araujo, I. Bayrak Pehlivan, T. Edvinsson, High-entropy alloy catalysts: Fundamental aspects, promises towards electrochemical NH3 production, and lessons to learn from deep neural networks, Nano Energy 105 (2023). https://doi.org/10.1016/j.nanoen.2022.108027.

[22] J. Hao, Z. Zhuang, K. Cao, G. Gao, C. Wang, F. Lai, S. Lu, P. Ma, W. Dong, T. Liu, M. Du, H. Zhu, Unraveling the electronegativity-dominated intermediate adsorption on high-entropy alloy electrocatalysts, Nat Commun 13 (2022). https://doi.org/10.1038/s41467-022-30379-4.

[23] Y. Sun, S. Dai, High-entropy materials for catalysis: A new frontier, Sci Adv 7 (2021). https://doi.org/10.1126/sciadv.abg1600.

[24] N.L. Okamoto, K. Yuge, K. Tanaka, H. Inui, E.P. George, Atomic displacement in the CrMnFeCoNi high-entropy alloy - A scaling factor to predict solid solution strengthening, AIP Adv 6 (2016). https://doi.org/10.1063/1.4971371.

[25] G. Arora, S. Kamrava, P. Tahmasebi, D.S. Aidhy, Charge-density based convolutional neural networks for stacking fault energy prediction in concentrated alloys, Materialia (Oxf) 26 (2022). https://doi.org/10.1016/j.mtla.2022.101620.

[26] G. Arora, A. Manzoor, D.S. Aidhy, Charge-density based evaluation and prediction of stacking fault energies in Ni alloys from DFT and machine learning, J Appl Phys 132 (2022). https://doi.org/10.1063/5.0122675.

[27] S. Zhao, T. Egami, G.M. Stocks, Y. Zhang, Effect of d electrons on defect properties in equiatomic NiCoCr and NiCoFeCr concentrated solid solution alloys, Phys Rev Mater 2 (2018). https://doi.org/10.1103/PhysRevMaterials.2.013602.

[28] G. Kresse, J. Furthmüller, Efficiency of ab-initio total energy calculations for metals and semiconductors using a plane-wave basis set, Comput Mater Sci 6 (1996) 15–50. https://doi.org/https://doi.org/10.1016/0927-0256(96)00008-0.

[29] G. Kresse, J. Furthmüller, Efficient iterative schemes for ab initio total-energy calculations using a plane-wave basis set, Phys Rev B 54 (1996) 11169–11186. https://doi.org/10.1103/PhysRevB.54.11169.

[30] G. Kresse, J. Hafner, Ab initio molecular dynamics for liquid metals, Phys Rev B 47 (1993) 558–561. https://doi.org/10.1103/PhysRevB.47.558.

[31] G. Kresse, D. Joubert, From ultrasoft pseudopotentials to the projector augmented-wave method, Phys Rev B 59 (1999) 1758–1775. https://doi.org/10.1103/PhysRevB.59.1758.

[32] A. van de Walle, Multicomponent multisublattice alloys, nonconfigurational entropy and other additions to the Alloy Theoretic Automated Toolkit, CALPHAD 33 (2009) 266–278. https://doi.org/10.1016/j.calphad.2008.12.005.

[33] C. Niu, C.R. LaRosa, J. Miao, M.J. Mills, M. Ghazisaeidi, Magnetically-driven phase transformation strengthening in high entropy alloys, Nat Commun 9 (2018). https://doi.org/10.1038/s41467-018-03846-0.

[34] D. Ma, B. Grabowski, F. Körmann, J. Neugebauer, D. Raabe, Ab initio thermodynamics of the CoCrFeMnNi high entropy alloy: Importance of entropy contributions beyond the configurational one, Acta Mater 100 (2015) 90–97. https://doi.org/10.1016/j.actamat.2015.08.050.

[35] A. Tamm, A. Aabloo, M. Klintenberg, M. Stocks, A. Caro, Atomic-scale properties of Ni-based FCC ternary, and quaternary alloys, Acta Mater 99 (2015) 307–312. https://doi.org/10.1016/j.actamat.2015.08.015.

[36] B. Yin, S. Yoshida, N. Tsuji, W.A. Curtin, Yield strength and misfit volumes of NiCoCr and implications for short-range-order, Nat Commun 11 (2020). https://doi.org/10.1038/s41467-020-16083-1.

[37] C. Niu, A.J. Zaddach, A.A. Oni, X. Sang, J.W. Hurt, J.M. Lebeau, C.C. Koch, D.L. Irving, Spin-driven ordering of Cr in the equiatomic high entropy alloy NiFeCrCo, Appl Phys Lett 106 (2015). https://doi.org/10.1063/1.4918996.

[38] R.F.W. Bader, Atoms in Molecules: A Quantum Theory, Clarendon Press, 1990. https://books.google.com/books?id=up1pQgAACAAJ.

[39] G. Henkelman, A. Arnaldsson, H. Jónsson, A fast and robust algorithm for Bader decomposition of charge density, Comput Mater Sci 36 (2006) 354–360. https://doi.org/10.1016/j.commatsci.2005.04.010.

[40] A. Goyal, Y. Li, A. Chernatynskiy, J.S. Jayashankar, M.C. Kautzky, S.B. Sinnott, S.R. Phillpot, The influence of alloying on the stacking fault energy of gold from density functional theory calculations, Comput Mater Sci 188 (2021). https://doi.org/10.1016/j.commatsci.2020.110236.

[41] S.L. Shang, W.Y. Wang, B.C. Zhou, Y. Wang, K.A. Darling, L.J. Kecskes, S.N. Mathaudhu, Z.K. Liu, Generalized stacking fault energy, ideal strength and twinnability of dilute Mg-based alloys: A first-principles study of shear deformation, Acta Mater 67 (2014) 168–180. https://doi.org/10.1016/j.actamat.2013.12.019.

[42] P. Tu, Y. Zheng, C. Zhuang, X. Zeng, H. Zhu, A high-throughput computation framework for generalized stacking fault energies of pure metals, Comput Mater Sci 159 (2019) 357–364. https://doi.org/10.1016/j.commatsci.2018.12.013.

[43] S.L. Shang, W.Y. Wang, Y. Wang, Y. Du, J.X. Zhang, A.D. Patel, Z.K. Liu, Temperature-dependent ideal strength and stacking fault energy of fcc Ni: A first-principles study of shear deformation, Journal of Physics Condensed Matter 24 (2012). https://doi.org/10.1088/0953-8984/24/15/155402.

[44] S. Zhao, G.M. Stocks, Y. Zhang, Stacking fault energies of face-centered cubic concentrated solid solution alloys, Acta Mater 134 (2017) 334–345. https://doi.org/10.1016/j.actamat.2017.05.001.

[45] J. Ding, Q. Yu, M. Asta, R.O. Ritchie, Tunable stacking fault energies by tailoring local chemical order in CrCoNi medium-entropy alloys, Proc Natl Acad Sci U S A 115 (2018) 8919–8924. https://doi.org/10.1073/pnas.1808660115.

[46] S.L. Shang, J. Shimanek, S. Qin, Y. Wang, A.M. Beese, Z.K. Liu, Unveiling dislocation characteristics in N i3Al from stacking fault energy and ideal strength: A first-principles study via pure alias shear deformation, Phys Rev B 101 (2020). https://doi.org/10.1103/PhysRevB.101.024102.

[47] X. Zhang, B. Grabowski, F. Körmann, A. V. Ruban, Y. Gong, R.C. Reed, T. Hickel, J. Neugebauer, Temperature dependence of the stacking-fault Gibbs energy for Al, Cu, and Ni, Phys Rev B 98 (2018). https://doi.org/10.1103/PhysRevB.98.224106.

[48] D.J. Siegel, Generalized stacking fault energies, ductilities, and twinnabilities of Ni and selected Ni alloys, Appl Phys Lett 87 (2005) 1–3. https://doi.org/10.1063/1.2051793.

[49] M. Chandran, S.K. Sondhi, First-principle calculation of stacking fault energies in Ni and Ni-Co alloy, in: J Appl Phys, 2011. https://doi.org/10.1063/1.3585786.

[50] W. Li, X. Peng, A.H.W. Ngan, J.A. El-Awady, Surface energies and relaxation of NiCoCr and NiFeX (X = Cu, Co or Cr) equiatomic multiprincipal element alloys from first principles calculations, Model Simul Mat Sci Eng 30 (2022). https://doi.org/10.1088/1361-651X/ac3e07.

[51] G. Arora, D.S. Aidhy, Machine learning enabled prediction of stacking fault energies in concentrated alloys, Metals (Basel) 10 (2020) 1–17. https://doi.org/10.3390/met10081072.

[52] N. Papior, sisl: v<fill-version>, (2023). https://doi.org/10.5281/zenodo.597181.

[53] J. Schindelin, I. Arganda-Carreras, E. Frise, V. Kaynig, M. Longair, T. Pietzsch, S. Preibisch, C. Rueden, S. Saalfeld, B. Schmid, J.Y. Tinevez, D.J. White, V. Hartenstein, K. Eliceiri, P. Tomancak, A. Cardona, Fiji: An open-source platform for biological-image analysis, Nat Methods 9 (2012) 676–682. https://doi.org/10.1038/nmeth.2019.

[54] J. Pijuan, C. Barceló, D.F. Moreno, O. Maiques, P. Sisó, R.M. Marti, A. Macià, A. Panosa, In vitro cell migration, invasion, and adhesion assays: From cell imaging to data analysis, Front Cell Dev Biol 7 (2019). https://doi.org/10.3389/fcell.2019.00107.

[55] J.W. Boley, E.L. White, R.K. Kramer, Mechanically sintered gallium-indium nanoparticles, Advanced Materials 27 (2015) 2355–2360. https://doi.org/10.1002/adma.201404790.

[56] Y. Ikeda, F. Körmann, I. Tanaka, J. Neugebauer, Impact of chemical fluctuations on stacking fault energies of CrCoNi and CrMnFeCoNi high entropy alloys from first principles, Entropy 20 (2018). https://doi.org/10.3390/e20090655.

[57] P. Singh, S. Picak, A. Sharma, Y.I. Chumlyakov, R. Arroyave, I. Karaman, D.D. Johnson, Martensitic Transformation in FexMn80-xCo10Cr10 High-Entropy Alloy, Phys Rev Lett 127 (2021). https://doi.org/10.1103/PhysRevLett.127.115704.

[58] Y.C. Yang, C. Liu, C.Y. Lin, Z. Xia, Core effect of local atomic configuration and design principles in AlxCoCrFeNi high-entropy alloys, Scr Mater 178 (2020) 181–186. https://doi.org/10.1016/j.scriptamat.2019.11.016.

[59] S. Zhao, Y. Osetsky, G.M. Stocks, Y. Zhang, Local-environment dependence of stacking fault energies in concentrated solid-solution alloys, NPJ Comput Mater 5 (2019). https://doi.org/10.1038/s41524-019-0150-y.

[60] R. Zhang, S. Zhao, J. Ding, Y. Chong, T. Jia, C. Ophus, M. Asta, R.O. Ritchie, A.M. Minor, Short-range order and its impact on the CrCoNi medium-entropy alloy, Nature 581 (2020) 283–287. https://doi.org/10.1038/s41586-020-2275-z.

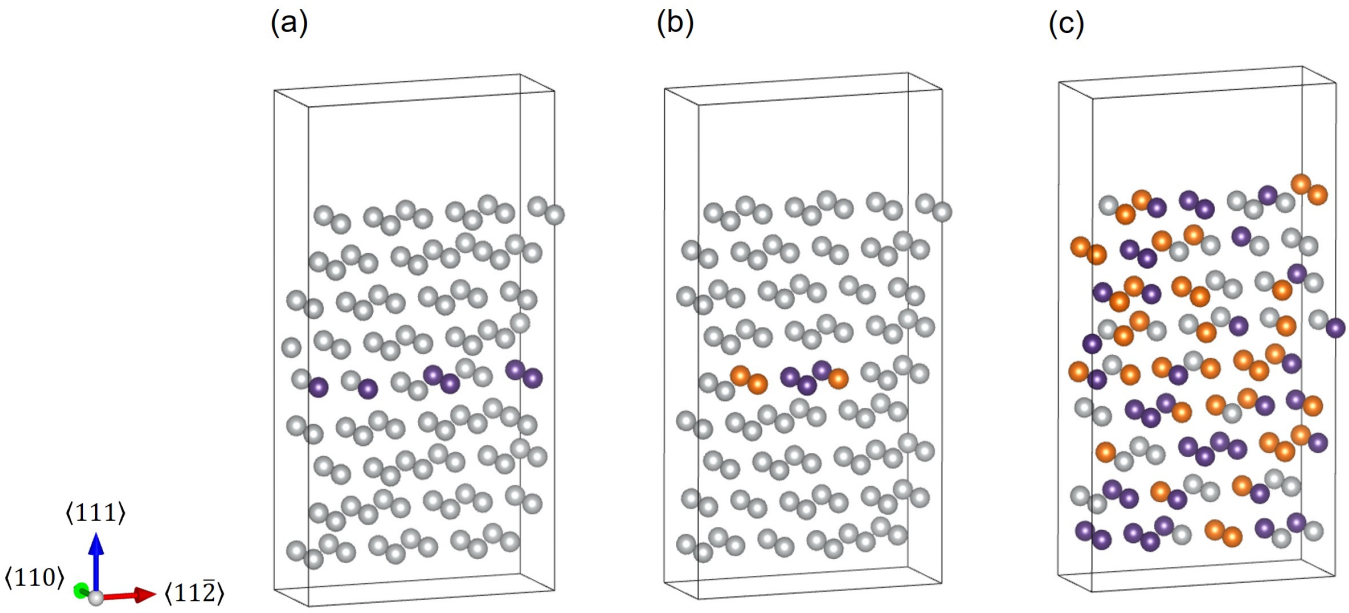

Figure 1. Supercells used for calculations of intrinsic SFEs in (a) dilute binaries (b) dilute ternaries, and (c) concentrated SQS ternary structures. Silver represents Ni host atoms while the orange and purple atoms are representative of the different alloying elements (Co, Fe, or Cr). In (a) and (b), alloying elements are added in the 5th layer only. See text for details.

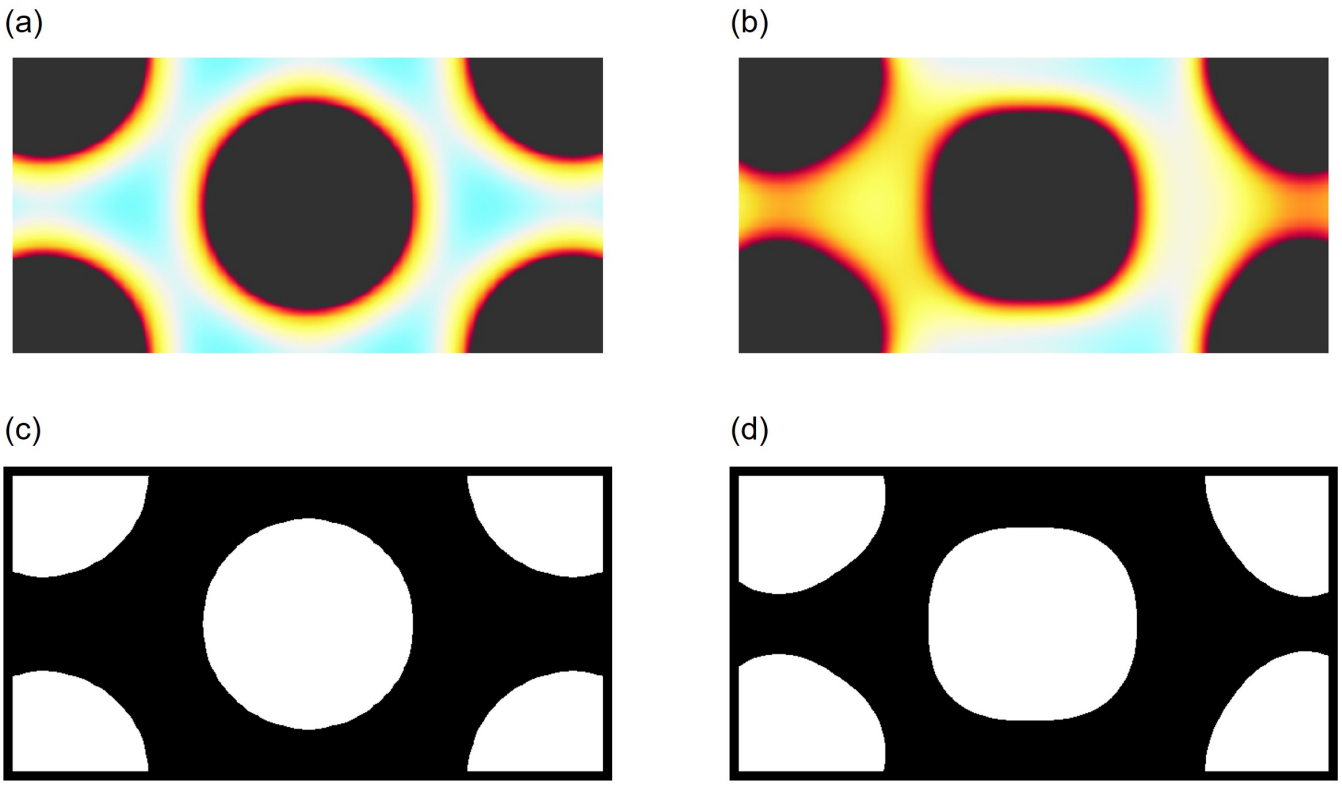

Figure 2. Preprocessed charge density images of (a) Ni and (b) Cr in a dilute NiCr alloy produced with sisl. (c) and (d) represent the converted grayscale images of Ni and Cr, respectively. These images are used to analyze the atomic charge and distortion, and to calculate the atomic area.

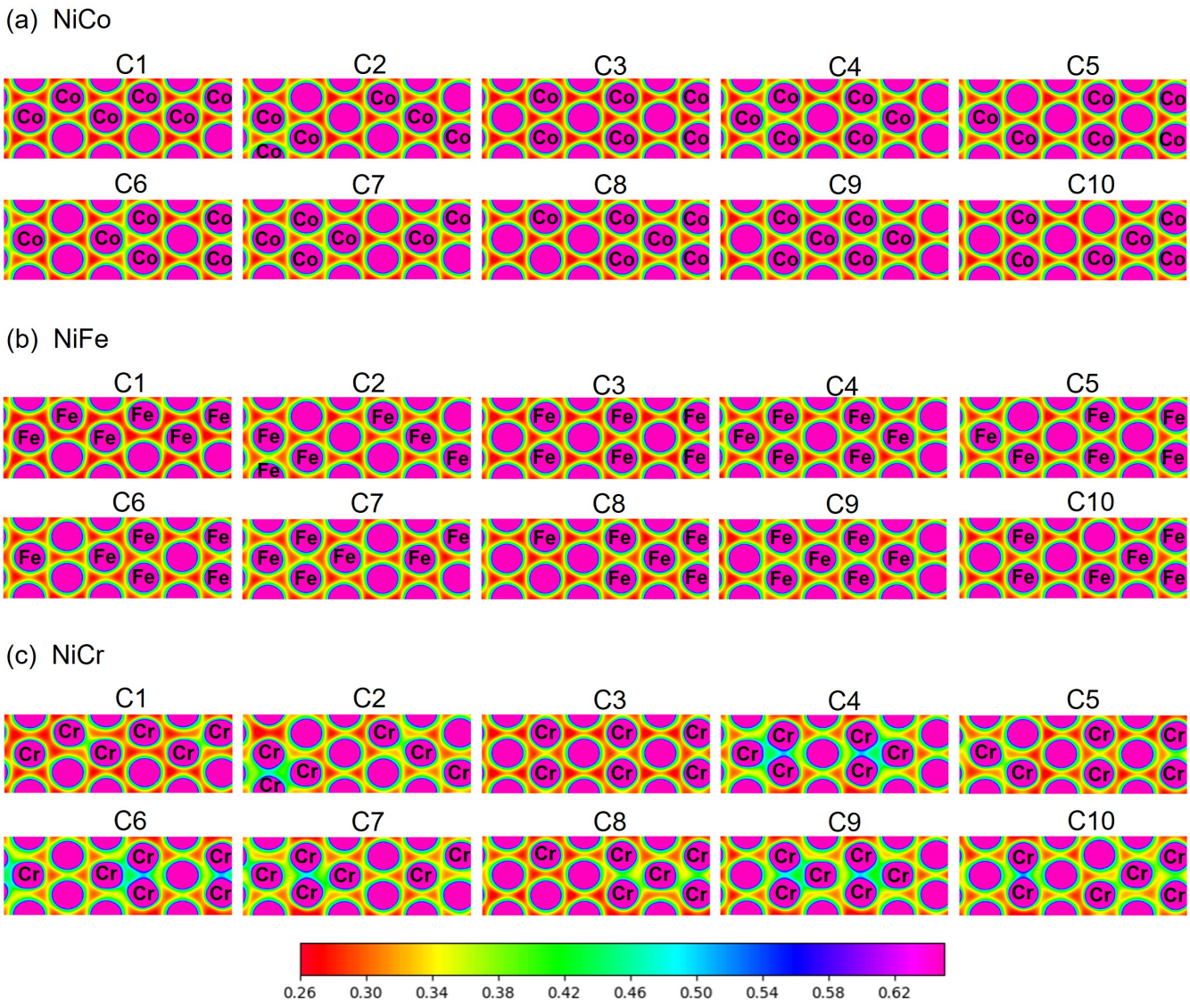

Figure 3. Charge density distribution in binary dilute alloys namely, (a) NiCo, (b) NiFe, and (c) NiCr. Each of the ten configurations have a total of six alloying atoms placed in the 5th layer. Unlabeled atoms are Ni. A higher charge distortion is observed in NiCr compared to NiFe and NiCo.

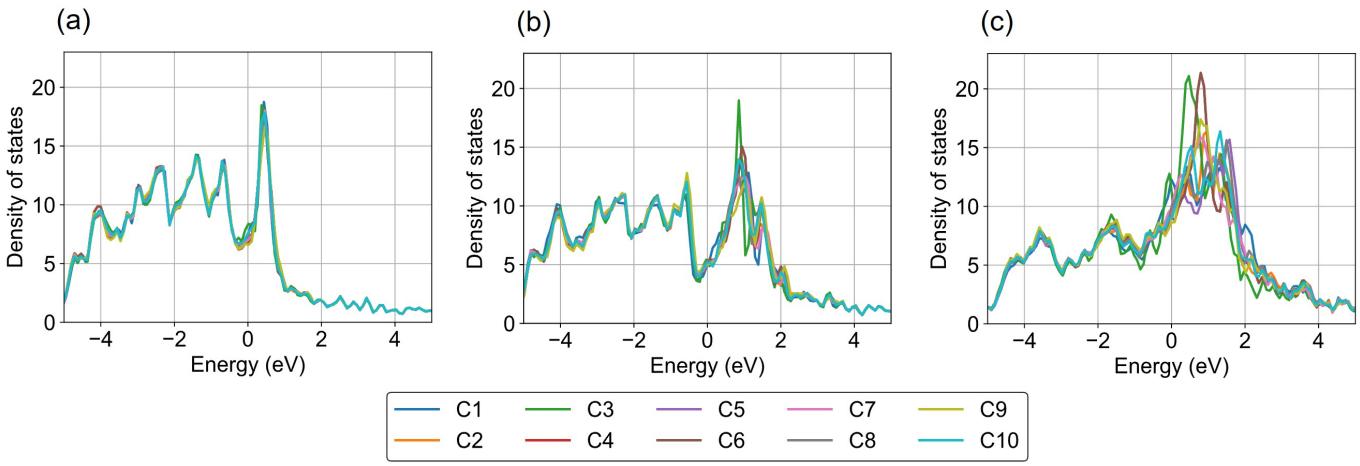

Figure 4. Projected DOS of (a) Co in NiCo, (b) Fe in NiFe, and (c) Cr in NiCr for all ten dilute-binary supercells as in Figure 1a. The Fermi level is set to 0 eV.

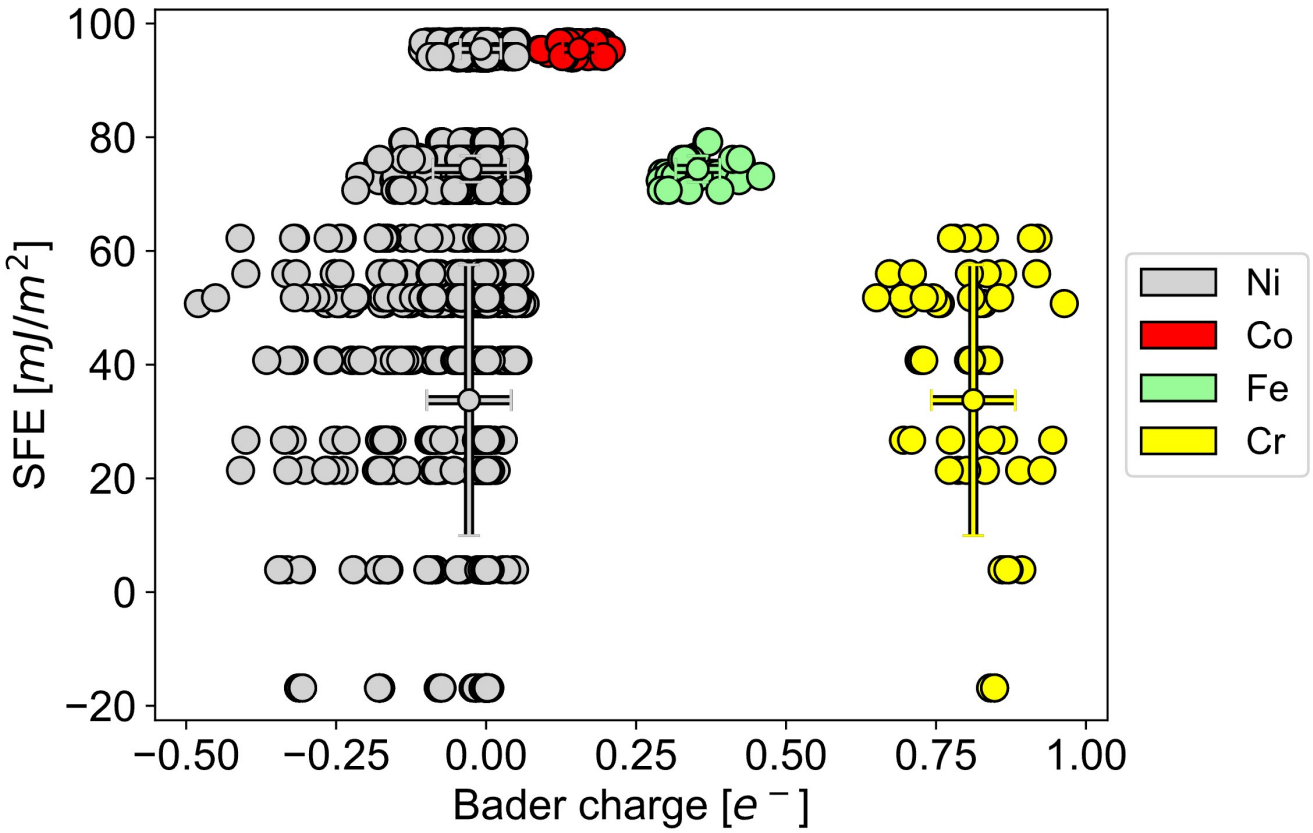

Figure 5. Bader charge of each atom in the ten supercells each of NiCo, NiFe and NiCr in Figure 1a. The corresponding SFEs of each supercell are also shown. Wide SFE and Bader charge variation in NiCr is observed compared to the NiFe and NiCo.

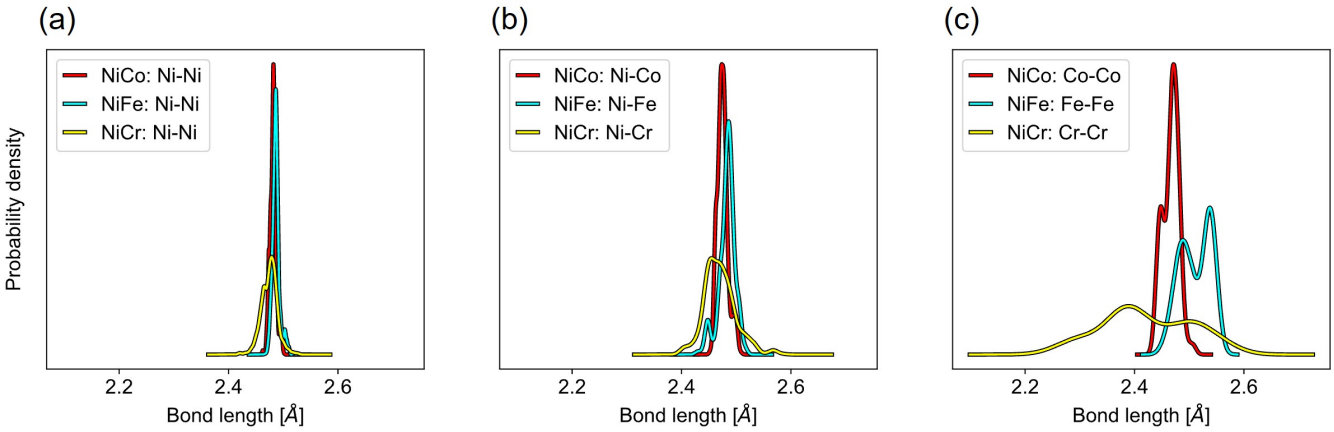

Figure 6. Bond length distributions in NiCo, NiFe, and NiCr dilute-binary structures. The bond lengths considered are the three 1NN bond types: (a) Ni-Ni, (b) Ni-X, (c) X-X, where X is the respective alloying element, Fe, Co or Cr in each alloy. Ni-Cr has a much larger bond length distribution, as observed in (c).

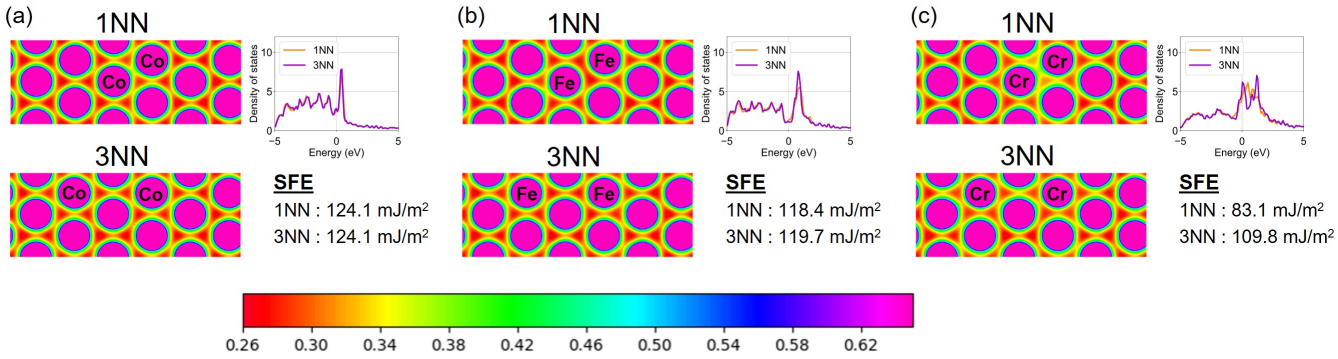

Figure 7. Comparison of charge density, DOS and SFE between 1NN and 3NN configurations in (a) NiCo, (b) NiFe, and (c) NiCr. Significantly higher variations for all three quantities are observed in NiCr.

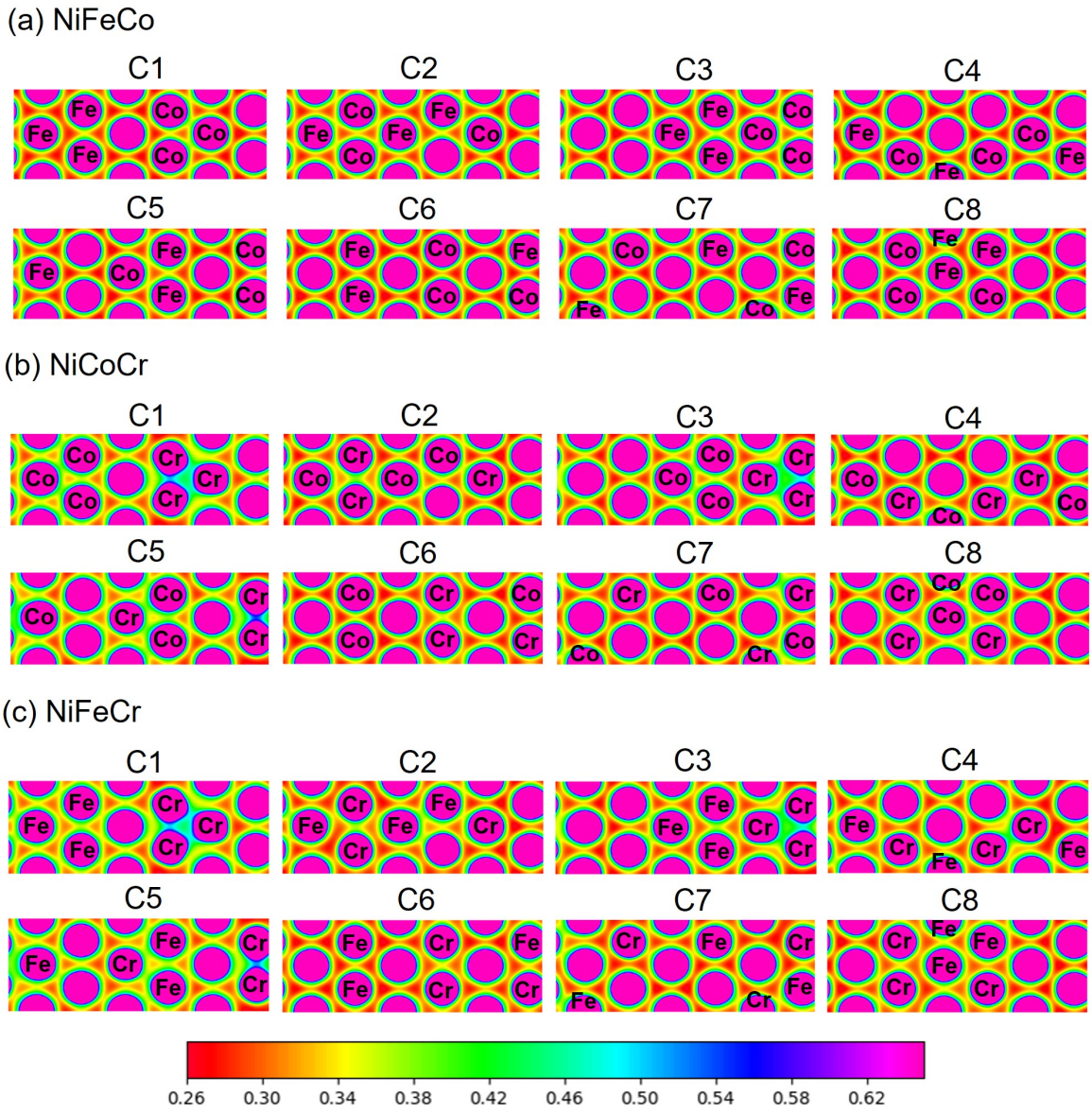

Figure 8. Charge density distributions in dilute ternary alloys: (a) NiFeCo, (b) NiCoCr, and (c) NiFeCr. Even with the addition of multiple alloying elements, alloys containing Cr display higher LCD. Areas in green and blue indicate areas of high charge density.

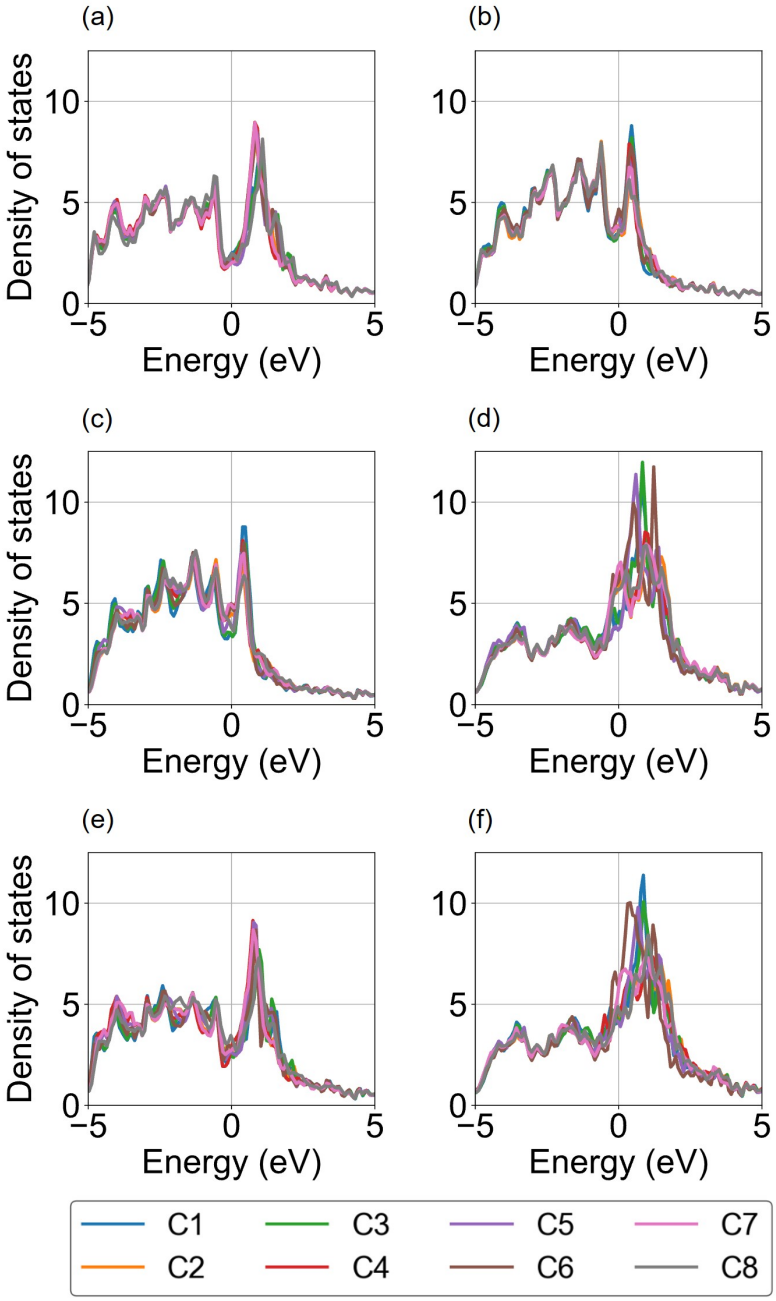

Figure 9. Projected DOS for (a) Fe and (b) Co atoms in NiFeCo, (c) Co and (d) Cr atoms in NiCoCr, and (e) Fe and (f) Cr atoms in NiFeCr in eight different configurations. The Fermi level is set to 0 eV for each alloy.

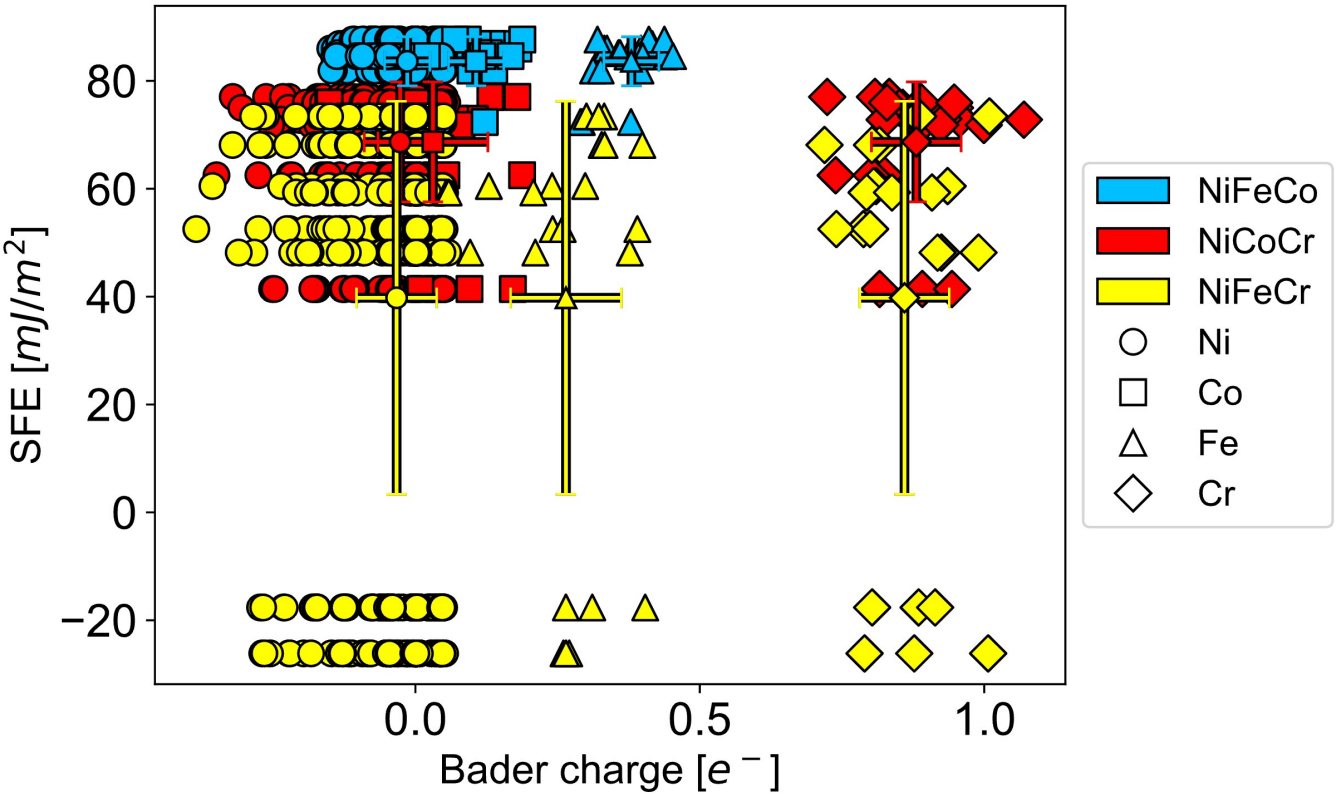

Figure 10. Bader charge of each atom in the eight configurations in NiFeCo, NiCoCr and NiFeCr with the corresponding supercell as shown in Figure 1b. The corresponding SFEs of each supercell are also shown. Wide SFE and Bader charge variation in NiFeCr and NiCoCr is observed compared NiFeCo.

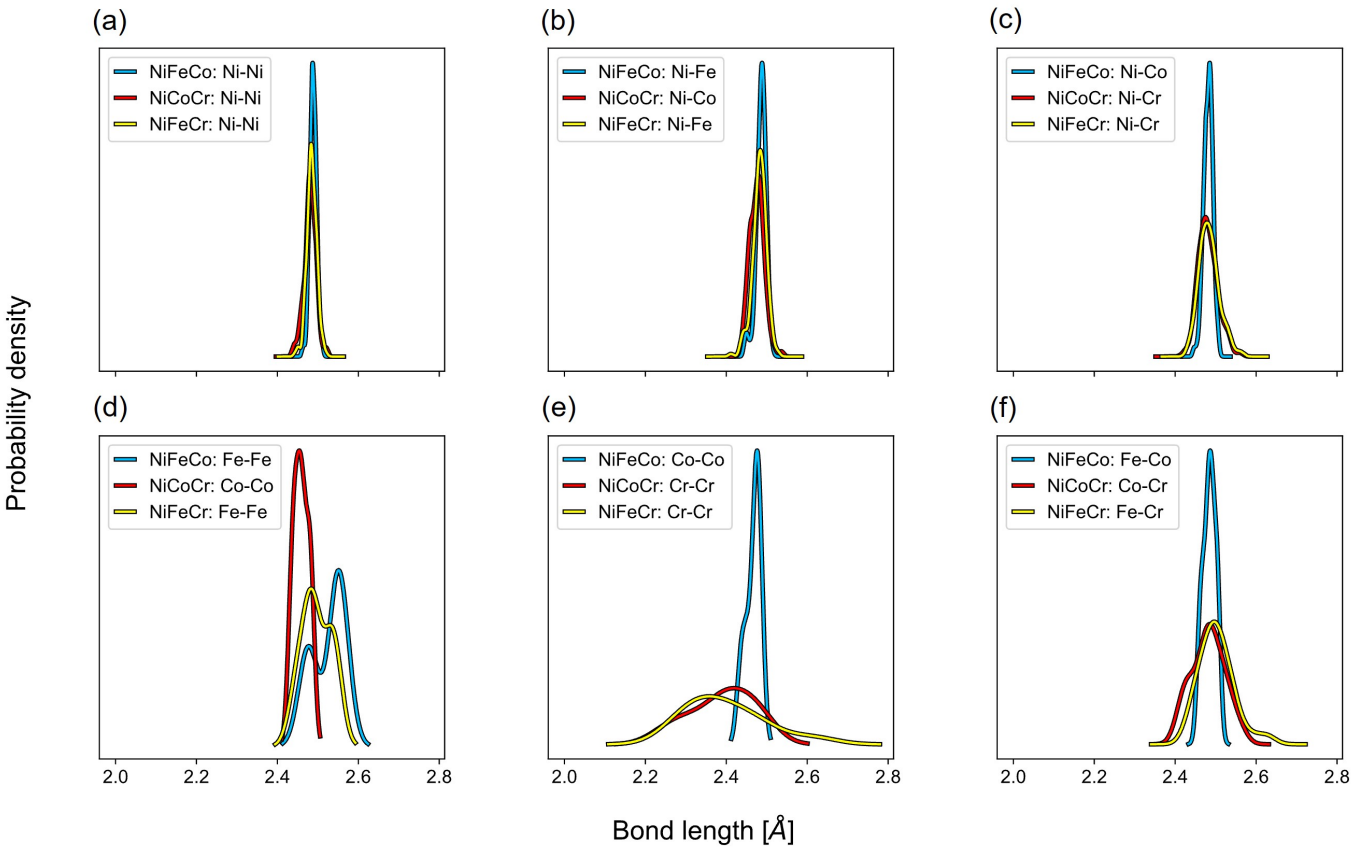

Figure 11. Bond length distribution for all dilute ternary alloys. Six 1NN bond types are considered for all structures: (a) Ni-Ni, (b) Ni-X_1, (c) Ni-X_2, (d) X_1-X_1, (e) X_2-X_2, (f) X_1-X_2 where X_1 and X_2 represent the distinct alloying elements for each structure.

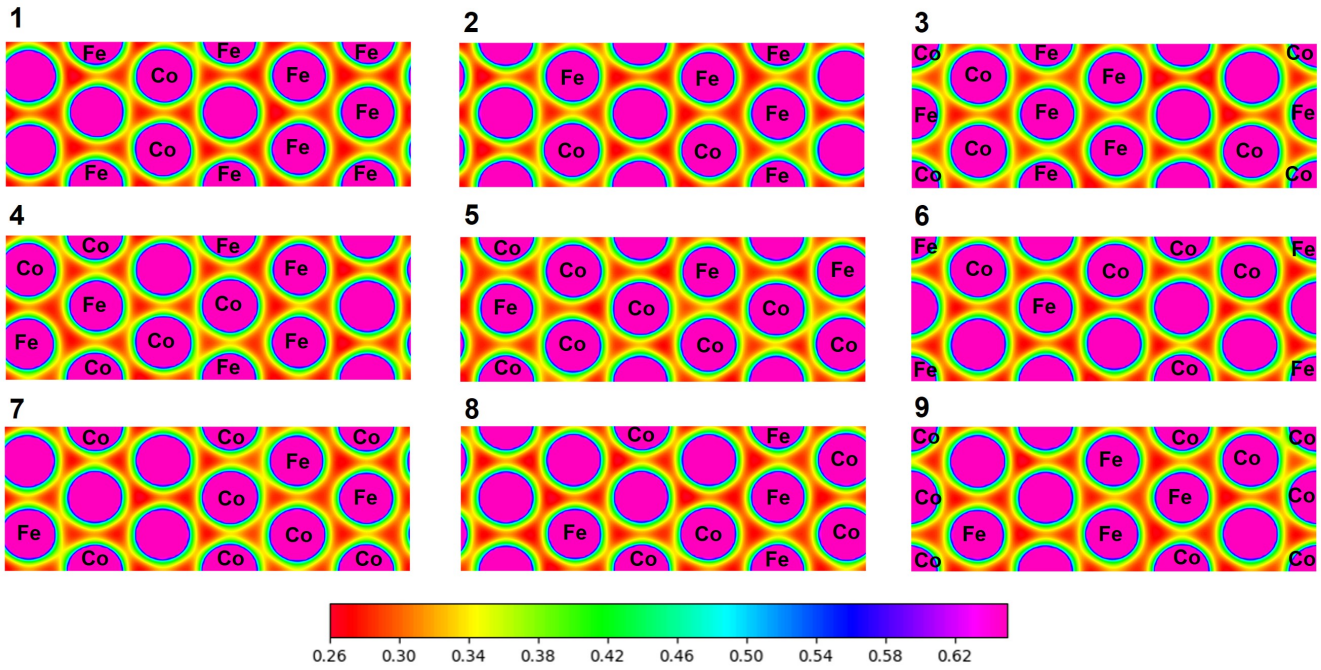

Figure 12. Charge density distributions of all nine layers in NiFeCo SQS ternary structure.

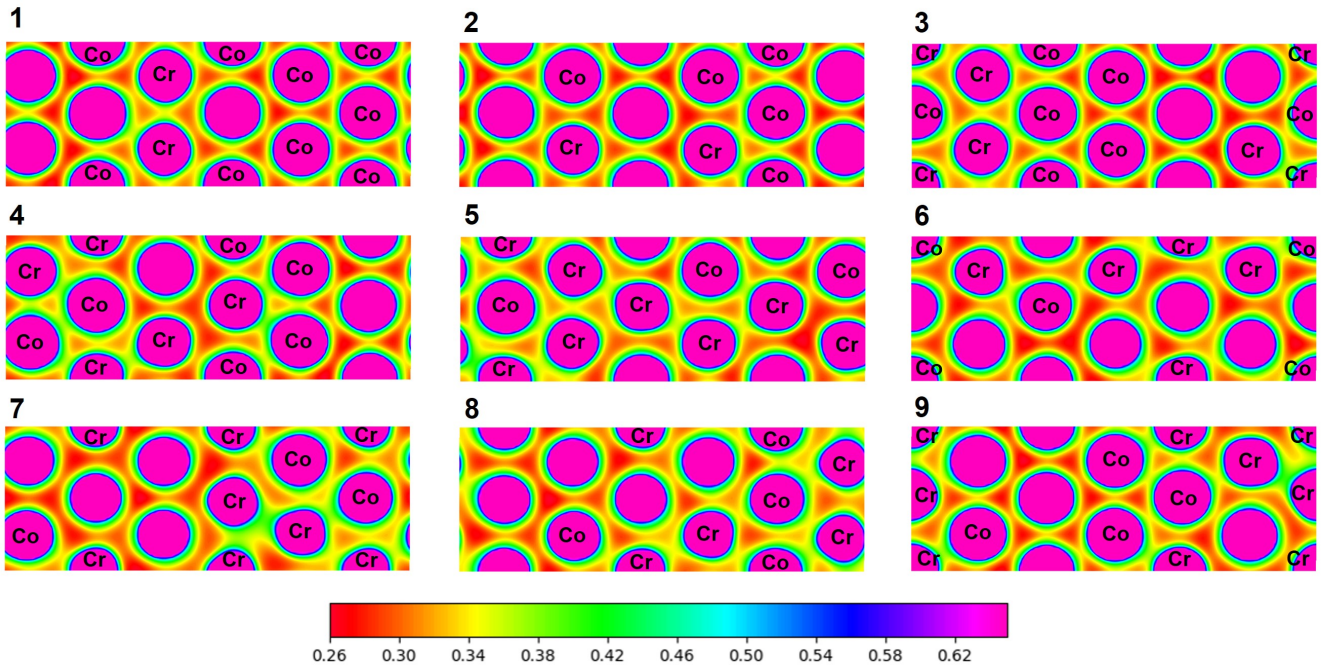

Figure 13. Charge density distributions of all nine layers in NiCoCr SQS ternary structure.

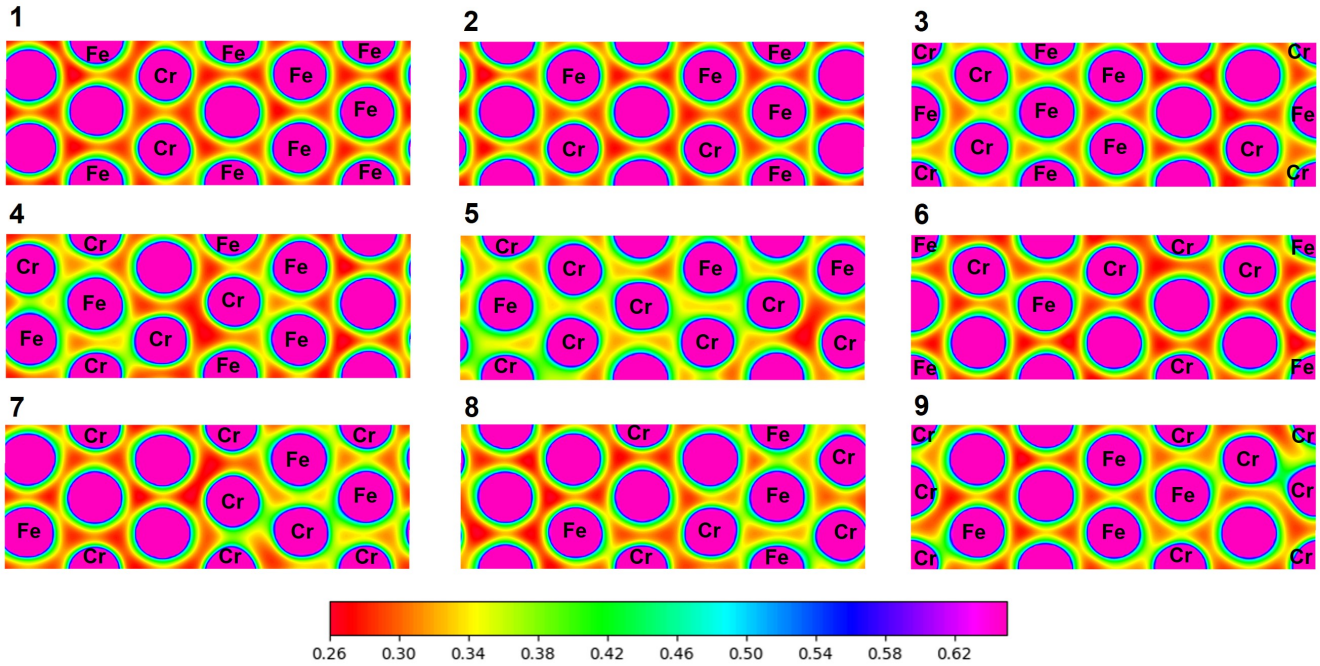

Figure 14. Charge density distributions of all nine layers in NiFeCr SQS ternary structure.

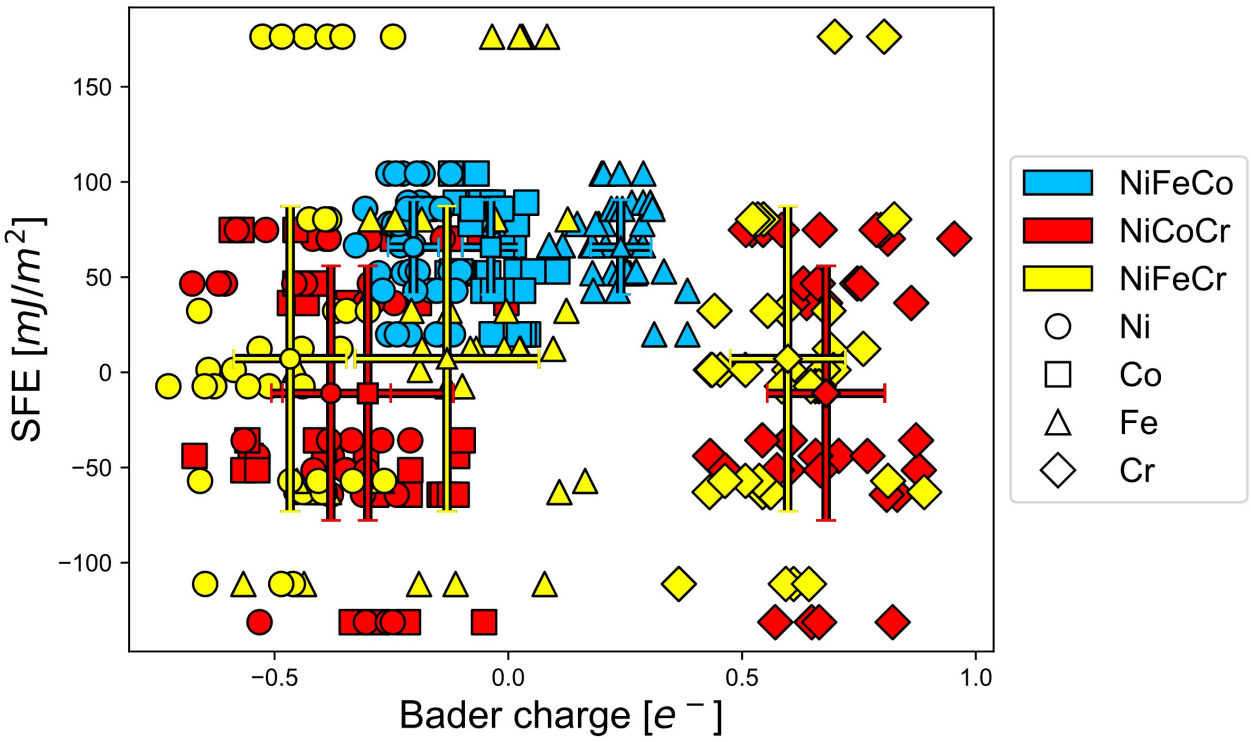

Figure 15. Comparison of SFE and Bader charge variations among NiFeCo, NiCoCr and NiFeCr in the three SQS ternary alloys. The SFEs were calculated for all nine layers in each supercell shown in Figure 1c.

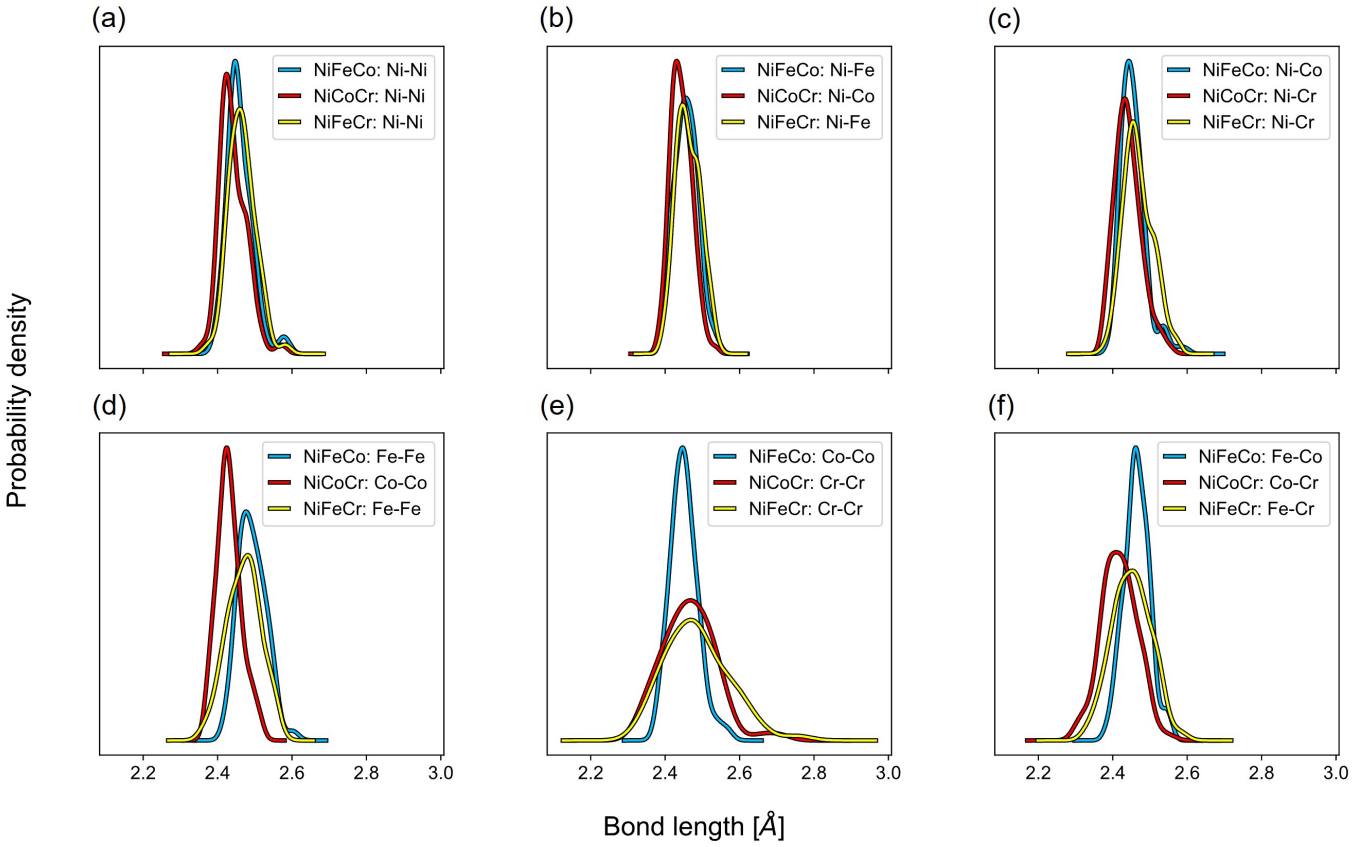

Figure 16. Bond length distribution for all concentrated ternary alloys. Six 1NN bond types are considered for all structures: (a) Ni-Ni, (b) Ni-X_1, (c) Ni-X_2, (d) X_1-X_1, (e) X_2-X_2, (f) X_1-X_2 where X_1 and X_2 represent the distinct alloying elements for each structure.

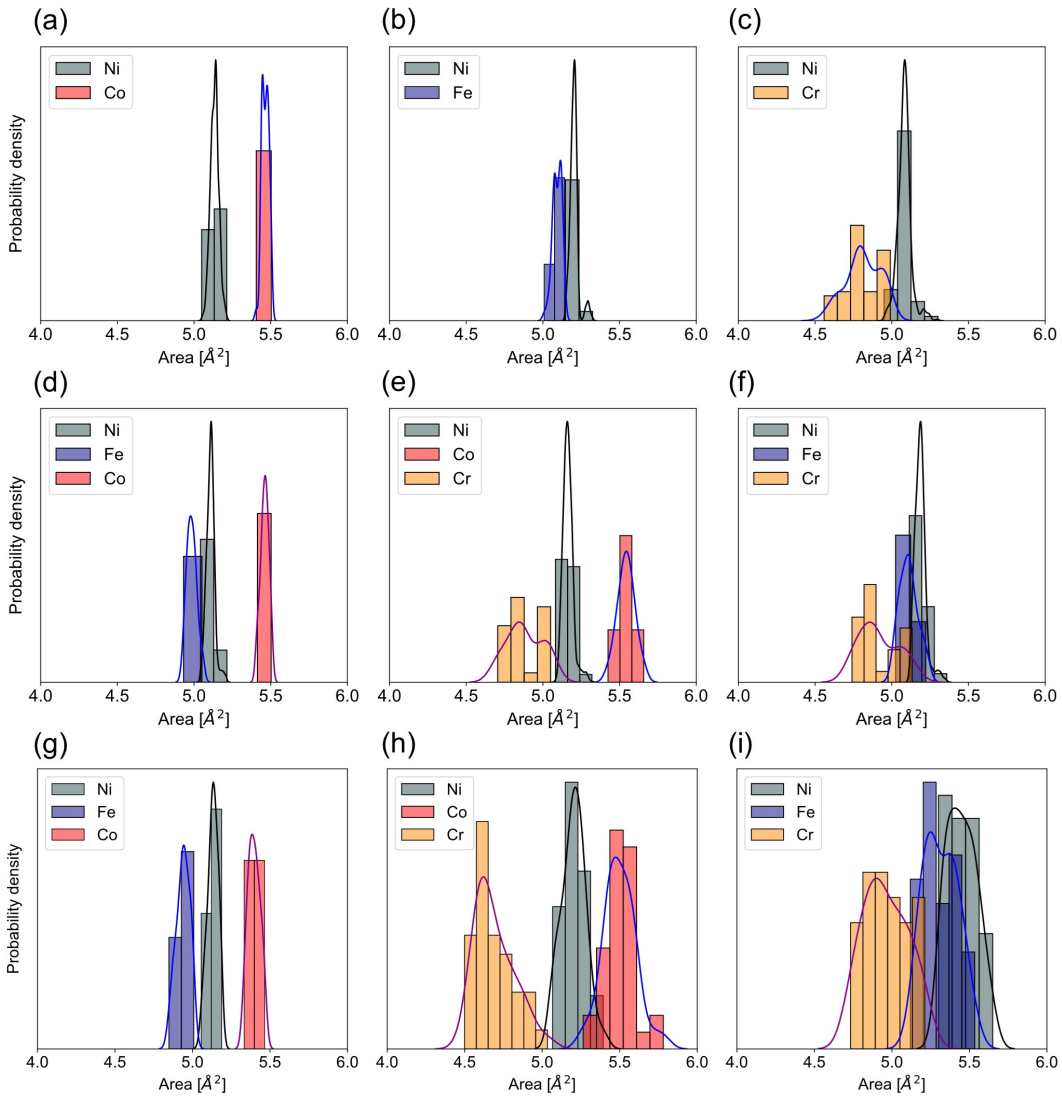

Figure 17. Charge density areas of the atoms in (a-c) dilute binaries, (d-f) dilute ternaries, and (g-i) SQS structures caused by LCD. Wider atomic area distributions are observed in all Cr-containing alloys.

Table 1. SFE values for all ten configurations of NiCo, NiFe, and NiCr dilute binary alloys.

Configuration	NiCo (mJ/m^2)	NiFe (mJ/m^2)	NiCr (mJ/m^2)
C1	94.313	76.48	3.927
C2	96.625	73.657	56.003
C3	93.969	79.164	-16.859
C4	96.764	73.603	40.78
C5	95.981	75.556	62.243
C6	96.693	73.488	40.752
C7	94.756	72.357	26.717
C8	95.426	73.122	50.745
C9	96.64	70.678	51.763
C10	94.178	76.108	21.415

Table 2. SFE values for all eight configurations of NiFeCo, NiCoCr, and NiFeCr dilute ternary alloys.

Configuration	NiFeCo (mJ/m^2)	NiCoCr (mJ/m^2)	NiFeCr (mJ/m^2)
C1	85.992	77.023	68.118
C2	84.524	75.009	60.506
C3	81.922	62.505	52.527
C4	86.845	72.969	73.412
C5	85.155	72.803	-26.139
C6	87.664	41.417	-17.626
C7	84.595	71.828	48.171
C8	72.375	75.963	59.304

Table 3. SFE values for all nine layers of NiFeCo, NiCoCr, and NiFeCr SQS concentrated ternary alloys.

Layer	NiFeCo (mJ/m^2)	NiCoCr (mJ/m^2)	NiFeCr (mJ/m^2)
1	66.683	-64.289	12.344
2	104.397	70.18	176.292
3	77.941	36.39	80.34
4	52.0572	-43.927	-111.177
5	89.127	74.779	1.268
6	19.935	46.628	-7.319
7	52.978	-51.434	-62.919
8	42.859	-35.738	-57.039
9	85.868	-131.244	32.304